Shallow-Water Bathymetry Retrieval Based on an Improved Deep Learning Method Using GF-6 Multispectral Imagery in Nanshan Port Waters

Wei Shen, Muyin Chen, Zhongqiang Wu, *Member, IEEE*, and Jiaqi Wang

***Abstract*—In a seaport, accurate bathymetric maps are valuable for both environmental and economic reasons. One of the main complementary methods for measuring shallow-water depth is the retrieval of the water depth by satellite. The results of the water depth inversion are greatly influenced by factors related to water quality. The proposed updated quasi-analysis algorithm (UQAA) allows for the calculation of water quality factors, and their spatial distribution characteristic strongly correlates with the trend in water depth distribution. By using satellite-derived bathymetry, these parameters can be used in the model training to extract the underwater terrain. This article proposes the idea of combining the UQAA with a convolutional neural network (CNN) based deep learning framework to retrieve the depth of the water and automatically extract the underwater terrain. We compare four different existing machine learning algorithms as baselines, using GF-6 multispectral remote-sensing images and in situ depth data in Nanshan Port as a priori validation set. We find that the result of the CNN model using the UQAA is better than other baselines, where the root-mean-square error was down to 0.55 m, the mean relative error was 6.63%, and the R^2 was 0.92. The developed method, which introduces the water quality factors containing geographic information as feature quantities, provides a new direction for further improvement.**

***Index Terms*—Bathymetry, convolutional neural networks (CNNs), deep learning, GF-6, inherent optical properties (IOPs).**

I. Introduction

ACCURATE bathymetric mapping plays a crucial role in environmental conservation, resource utilization, and efficient port management. Shallow-water depth information is essential for informed decision making and supports various human activities, contributing to both environmental sustainability and economic prosperity in seaport regions [1].

Mapping shallow-water depth in port areas is of utmost importance for various maritime activities. Traditionally, sound navigation and ranging (SONAR) and light detection and ranging (LiDAR) have been employed for this purpose. However, these methods have limitations in terms of cost and spatial coverage [2]. SONAR technology exhibits high operational efficiency but is limited in its applicability for large-scale usage due to its high cost. On the other hand, LiDAR technology offers a cost-effective solution for bathymetric applications, albeit with relatively lower operational efficiency compared at the same time.

The implementation of satellite-derived bathymetry (SDB) revolutionizes the mapping of shallow-water depths in port areas, facilitating improved navigation safety, port management, and coastal zone planning. Its cost effectiveness and spatial-extensive nature make it an attractive choice for monitoring and managing shallow-water areas. It has made great technological advances since the launch of artificial satellites and the rapid development of computer science. It has become one of the main complementary means for shallow-water depth measurement due to the advantages of repeatable observation, wide view, and low cost.

Different wavelengths of light have different reflectances when penetrating water. Based on this principle, remote-sensing satellite data can be utilized to retrieve the water depth. The traditional SDB methods are generally categorized as physics-based methods and empirical methods. The first method focuses on the interaction of light in water from a theoretical perspective [3], [4], whereas the second method investigates the empirical relationship between the spectral radiation patterns and the optical parameters. By using a logarithmic conversion ratio model to retrieve the water depth, it is found to reduce the impact of different sediments in the shallow sea to a certain extent [5]. As we have mentioned, most traditional sounding algorithms do not consider the spatial correlation between sounding points and surrounding pixels. The linear relationship is not sufficient to investigate and extend the mathematical and physical relationship between the features and the labels.

Although building a universal algorithm to explain the relationship between multidimensional spectral value and in situ

Manuscript received 28 June 2023; revised 24 July 2023 and 2 August 2023; accepted 23 August 2023. Date of publication 30 August 2023; date of current version 22 September 2023. This work was supported in part by the Teaching Reform Research Project, Hainan Normal University under Grant hsjg2023-07, in part by the National Natrual Science Foundation of China under Grant 61991454, in part by the the Oceanic Interdisciplinary Program of Shanghai Jiao Tong University under Grant SL2022ZD206, in part by the the Scientific Research Fund of Second Institute of Oceanography, MNR under Grant SL2302, and in part by the National Key Research and Development Program of China under Grant 2016YFC1400901. *(Wei Shen and Muyin Chen are co-first authors.) (Corresponding author: Zhongqiang Wu.)*

Wei Shen is with the School of Marine Science, Shanghai Ocean University, Shanghai 201306, China, and also with the Marine Surveying and Mapping Engineering and Technology Research Center, Shanghai 201306, China (e-mail: wshen@shou.edu.cn).

Muyin Chen and Jiaqi Wang are with the School of Marine Science, Shanghai Ocean University, Shanghai 200090, China (e-mail: we4237@163.com; w735421738@163.com).

Zhongqiang Wu is with the School of Information Science and Technology, Hainan Normal University, Haikou 571158, China (e-mail: wuzhongqiang2008@qq.com).

Digital Object Identifier 10.1109/JSTARS.2023.3310166

data is challenging, statistical methods can be employed to investigate the numerical model and search for the optimal solution [6]. Various machine learning algorithms have been applied to the field of extraction of water depth and underwater terrain inversion. A support vector machine was employed to estimate water depth at two different ports in the cities of Luarca and Candás in the Principality of Asturias (Spain) [7]. Furthermore, there have been instances where these technologies have been applied to the port of China [8]. Through these studies, it is shown that, at this time, the empirical-based method is more applicable than the physic-based method in water areas with turbid and complex water environments, such as a port.

Deep learning frameworks have also been employed to improve the accuracy of inversion. Owing to their capabilities in image processing and feature analysis [9], [10], [11], deep learning techniques have gained significant attention in various Earth observation and remote-sensing applications. Chen et al. [12], [13] developed a deep learning model that integrated local aggregation and global attention mechanisms, which could effectively extract the spectral and spatial features of hyperspectral images by using a spectral-induced aligned superpixel segmentation technique and achieve high-accuracy classification results. The authors in [14] and [15] proposed a graph convolutional network for hyperspectral image classification, which can model the relations between samples using graph structures and improve the spatial–spectral feature representations. A cross-channel reconstruction module was introduced for multimodal remote-sensing data classification, which can exchange information between modalities by reconstruction strategy and learn more compact fusion representations [16]. A novel deep learning called grid network was proposed to rethink the feature extraction of hyperspectral images from anisotropic perspectives and to fully explore the spectral and spatial features in multistage and multipath processes [17].

In the context of port surveys, the wavelet neural network model was developed utilizing the spectral reflectance values obtained from top-of-atmosphere computations. The utilization of this neural network model demonstrated its effectiveness as a powerful tool in the field [18]. In the study, a convolutional neural network (CNN) was utilized to perform depth estimation in the Devil's Lake area (North Dakota, USA). The task of depth estimation was approached as a classification problem, leveraging the capabilities of the CNN architecture [19]. Furthermore, the accurate estimation of coastal water depth in the turbid water was achieved using Sentinel-2 Level 2A imagery, particularly in regions characterized by clear seawater [8]. Al Najar et al. [20] demonstrated a promising direction for the applicability of deep learning models in the field of marine surveying. Although they both use the deep learning framework, they are limited by the spectral information as the training data, which does not give full play to the huge potential of deep learning, and the results obtained still have room for improvement. Introducing water factors to improve the results was less studied before.

Many existing studies indicate that inherent optical properties (IOPs) can be referred as another candidate factor to improve SDB accuracy [21]. The value of IOPs exhibits significant variations with water depth, establishing a strong correlation between the spatial distribution of water quality and the distribution of water depth. Yang et al. [22] introduced IOPs in turbid waters to retrieve the euphotic zone depth in inland waters using a modified quasi-analytical algorithm (QAA). Zhang et al. [23] proposed a linear model known as the inherent optical parameter linear model (IOPIM) to estimate shallow-water depth using high-spatial-resolution multispectral images. The findings from the IOPIM study demonstrated the potential of using inherent optical parameters (IOPs) to enhance the accuracy of water depth estimation. Huang et al. [24] proposed an updated quasi-analytical algorithm (UQAA) and verified its feasibility. Wu et al. [25] calculated that the UQAA was raised to calculate the phytoplankton pigment absorption coefficient and the chlorophyll-a concentration, functioning as the characteristic factors of water depth estimation.

In this study, a novel framework was proposed that combines the UQAA with CNN. The authors aim to improve the accuracy and efficiency of the water depth inversion by combining the UQAA with a CNN-based deep learning framework. The UQAA can calculate the water quality factors that affect the water depth, and the CNN can automatically extract the underwater terrain features from the satellite images. The proposed model was compared with other four classical ML methods (i.e., the back-propagation neural network (BP-NN) [26], random forest (RF) [27], eXtreme Gradient Boosting (XGBoost) [28], and support vector regression (SVR) [7]) to verify the bathymetric ability. The results determine that the proposed framework outperforms other baseline cases. The concept of incorporating additional features beyond optical channels as supplementary training data can be extended to other geographical regions or scenarios that demand precise bathymetric mapping, including applications in coastal erosion monitoring, coral reef preservation, marine habitat mapping, and underwater archaeology. This approach holds the potential for enhancing the accuracy and applicability of bathymetric estimation in various environmental settings.

II. Data and Methods

The main body of the study consists of two steps: Data preprocessing and model training (see Fig. 1).

In the data preprocessing part, the remote-sensing data used in this study were acquired from the GF-6 wide-field-view (WFV) multispectral optical satellite, while the in situ measurement data were obtained from SONAR measurements. To enhance the accuracy of bathymetry estimation, the remote-sensing data underwent preprocessing steps, including radiation correction and flare removal. The estimation of Chlorophyll-a concentration (C) and the absorption coefficient of colored dissolved organic matter (CDOM) at 440 nm [$a_g(440)$] were conducted using the UQAA. Subsequently, bathymetric points were extracted from in situ SONAR data, serving as a priori information. All data were stored in floating-point format. Through resampling, the R_{rs} values for the blue, green, and red bands, along with the two water quality factors, were matched with control points derived from GF-6 images within a specified window size at each point.

In the model training part, the collected data were utilized in three distinct training methods, depending on specific

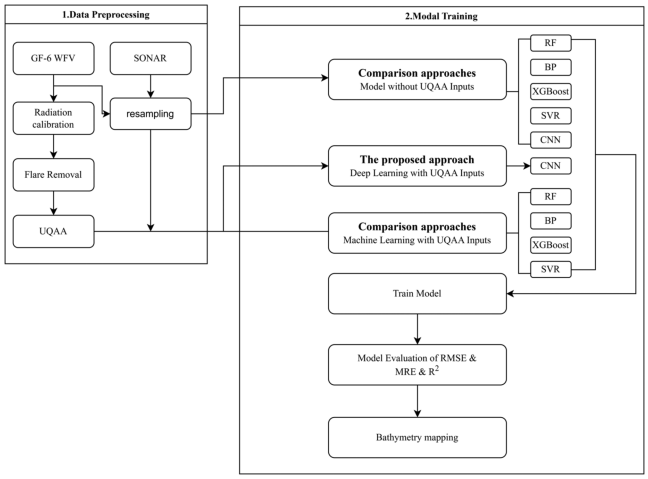

Fig. 1. General workflow of the proposed system by using different approaches.

Fig. 2. Study area at Nanshan port waters area.

conditions. Some SONAR data that were not incorporated into the network were reserved for validation purposes, enabling the evaluation of accuracy. Evaluation metrics, such as root-mean-square error (RMSE), mean relative error (MRE), and R^2 were employed to assess the accuracy of the bathymetry estimation in comparison with other baselines.

A. Data Preprocessing

1) Study Area: The article selects optical shallow-water areas of Nanshan Port within Sanya, Hainan province as the study area. The geolocation of the study area is shown in Fig. 2. The water quality in this area is clear, the seabed topography changes gently, and a small variety of bottom sediments. The water environmental conditions of Nanshan Port are typically characterized by turbidity. However, incorporating water quality factors can enhance the accuracy of bathymetric inversion. Therefore, the sea area of Nanshan Port was carefully selected to test the feasibility and accuracy of our proposed model. We conducted a qualitative evaluation of the variable bathymetry inversion model specifically for this region.

2) GF-6 WFV Data: We obtained GF-6 WFV images from the land observation satellite service [http://www.sasclouds.com/chinese/normal/ (accessed on July 17, 2021)]. Information on the GF-6 satellite is shown in Table I.

TABLE I
GF-6 IMAGE BAND INFORMATION

	Wide camera parameters	
Spectral region	blue	0.45–0.52 μm
	green	0.52–0.59 μm
	red	0.63–0.69 μm
	near-infrared	0.77–0.89 μm
	red-edge I	0.45–0.52 μm
	red-edge II	0.52–0.59 μm
	Coastal blue	0.40–0.45 μm
	yellow	0.59–0.63 μm
Spatial resolution	16 m	
Temporal resolution	4 days	

A resampling of the input GF image is done to match the same image dimension of the in situ data. The geographical location of each point is defined by its longitude and latitude. From the longitude and latitude, a coordinate projection is made using the WGS84 ellipsoid using geospatial data abstraction library package in Python. We reduce the spatial positioning error generated by projecting the measured points onto the image by minimizing E as much as possible

$$\mathbf{E} = \sum_{\boldsymbol{n}=1} (\boldsymbol{lon} - \boldsymbol{x})^2 + \sum_{\boldsymbol{n}\,=\,1} (\boldsymbol{lat} - \boldsymbol{y})^2 \tag{1}$$

a) Image preprocessing: The GF-6 image was radiometric calibrated using the FLAASH algorithm, while the glint effects were eliminated using Hedley's method [29], [30]. The state of the water surface will seriously affect the bathymetry of the shallow sea terrain. When there are wind waves in the scene, the solar flare on the water surface turns out to be very serious. It is necessary to eliminate the flare in the image such that the accuracy of water depth inversion can be improved. In this study, we employ Hedley's method to exploit the linear correlation between the reflectance values of the near-infrared band and other bands, aiming to mitigate the flare effects.

The image was resampled to a spatial resolution of 5 m by bilinear interpolation [31], the same as the in situ data. Finally, the corresponding reflectance data were taken as a part of the features.

To reduce information redundancy and the dimension of data, the optimum index factor (OIF) is often used to derive the optimal band feature combination [32]. The expression is given as follows:

$$R_{\mathrm{OIF}} = \frac{\boldsymbol{S}_1 + \boldsymbol{S}_2 + \boldsymbol{S}_3}{\boldsymbol{R}_{12} + \boldsymbol{R}_{13} + \boldsymbol{R}_{23}} \tag{2}$$

where S_1, S_2, and S_3 represent the standard deviations of any three wavebands, and R_{12}, R_{13}, and R_{23} represent the correlation coefficients between any three selected bands.

The basic principle behind this method is that the amount of information contained in an image is directly proportional to its standard deviation. A higher standard deviation indicates a larger amount of information. Conversely, the independence

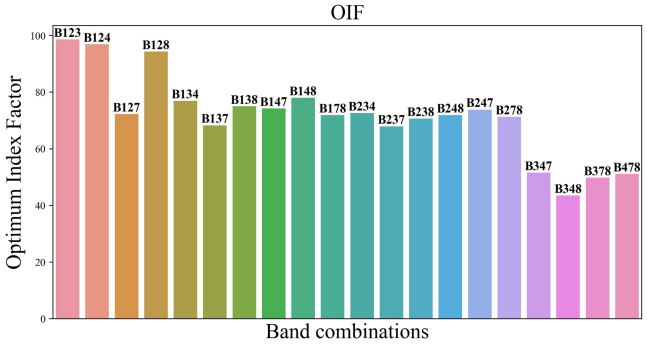

Fig. 3. OIFs of the GF-6 image.

of an image is inversely proportional to the correlation coefficient between its spectral bands. A lower correlation coefficient indicates a lower degree of information redundancy and better independence. This method combines the interband correlations and the information content of individual band images to achieve widespread application.

The fifth and sixth bands of the GF-6 image are the red edge bands, which are mainly used for the agricultural survey. They are not suitable for underwater information detection. We calculated the OIFs of the remaining six bands in Fig. 3. The first, second, and third bands of the GF-6 image are blue, green, and red bands, which were input into the training model. Moreover, these bands are like other satellites, which are better suited to verify the applicability of the UQAA.

b) Updated QAA: The QAA is a semianalytical model based on the bio-optical model proposed by Zhao et al. [26]. Regarding multispectral satellites on the market that only have three–four wavebands of valid ocean data, it is meaningful to limit the number of unknown parameters of the QAA as it reduces the impact of incorrect data on the model. It is shown by Mateo-Perez et al. [27] that the absorption coefficient of chlorophyll at 440 nm and the backscattering coefficients at 550 nm can be presented in terms of the chlorophyll-a concentration C as follows:

$$b_{bp}\left(\lambda_0 = 550\right) = 0.0111{*}C^{0.62} \tag{3}$$

$$a_{\text{phy}}(\lambda_1 = 440) = 0.06{*}C^{0.65}. \tag{4}$$

In clear water, we have the following:

$$b_{bp}\left(\lambda\right) = b_{bp}\left(\lambda_0\right)\left(\lambda_0/\lambda\right)^{Y}\ \left(Y{=}\ 0.67875\right) \tag{5}$$

$$b\left(\lambda\right) = b_w\left(\lambda\right) + b_{bp}\left(\lambda\right) \tag{6}$$

$$a_g\left(\lambda\right) = a_g\left(\lambda_1\right){*}\exp\left(-0.015{*}\left(\lambda - \lambda_1\right)\right) \tag{7}$$

$$a_{\text{phy}}\left(\lambda\right) = \left[a_0\left(\lambda\right) + a_1\left(\lambda\right)\ln\left(a_{\text{phy}}(\lambda_1)\right)\right]\ a_{\text{phy}}(\lambda_1) \tag{8}$$

$$a\left(\lambda\right) = a_w\left(\lambda\right) + a_{\text{phy}}\left(\lambda\right) + a_g\left(\lambda\right) \tag{9}$$

$$u\left(\lambda\right) = \frac{b\left(\lambda\right)}{a\left(\lambda\right) + b\left(\lambda\right)} \tag{10}$$

$$\lambda_0 = 550,\ \lambda_1 = 440. \tag{11}$$

Therefore, we can construct an equation equal to $u(\lambda)$ by using $a_g(440)$ and chlorophyll-a concentration C.

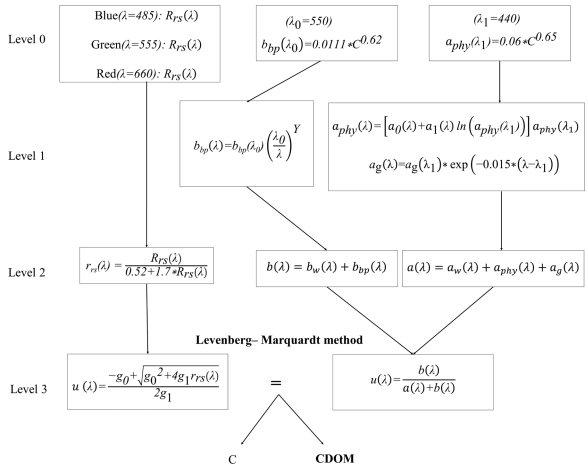

Fig. 4. Derivation process of UQAA.

Note that in the QAA, we have

$$r_{rs}\left(\lambda\right) = \frac{R_{rs}\left(\lambda\right)}{0.52 + 1.7R_{rs}\left(\lambda\right)} \tag{12}$$

$$u\left(\lambda\right) = \frac{-g_0 + \left[g_0^2 + 4g_1 r_{rs}\left(\lambda\right)\right]^{1/2}}{2g_1}. \tag{13}$$

Introducing R_{rs} from multispectral images, we can represent the below-surface remote-sensing reflectance (r_{rs}) and construct an equation set. In this set, g_0 and g_1 are the constants given by 0.08945 and 0.1247, respectively. The values a_0 and a_1 were from [33] by employing the interpolation function in MATLAB. The quantity a represents the total absorption coefficient of the water body, a_{phy} represents the absorption coefficient of chlorophyll, a_g represents the absorption coefficient of CDOM, which is represented by the $a_g(440)$, a_w represents the absorption coefficient of pure water, which is obtained directly, b_w represents the backscattering coefficient of pure water, which is obtained directly as well, b_{bp} represents the backscattering coefficient, which is represented by b_{bp} ($\lambda_0 = 550$), and λ represents the central wavelength of input bands.

Hypothetically, the difference between the actual value of subsurface R_{rs} of optical in deep water and the predicted value of the semianalytical method tends to be fairly slight. Hence, the optimum values of $a_g(440)$ and C can be solved by using the Levenberg–Marquardt method (see Fig. 4).

Fig. 5(a) and (b) shows that the water quality factors of Nanshan Port strongly correlate with the trend of water depth distribution. The nearshore, especially the port, is a high-value area of absorption coefficient, which is reflected in Fig. 5. When the mixing dilution effect of seawater is more obvious, the absorption coefficient value is smaller, so the absorption coefficient of deep water will be smaller [34]. The relative relationship between the absorption coefficient and the measured water depth is depicted in Fig. 5(c) and (d). The regression line, represented by a thick red line, is shown to align with the theoretically inferred distribution pattern. The results of UQAA contain obvious data information, which may be introduced into the detection of underwater topography.

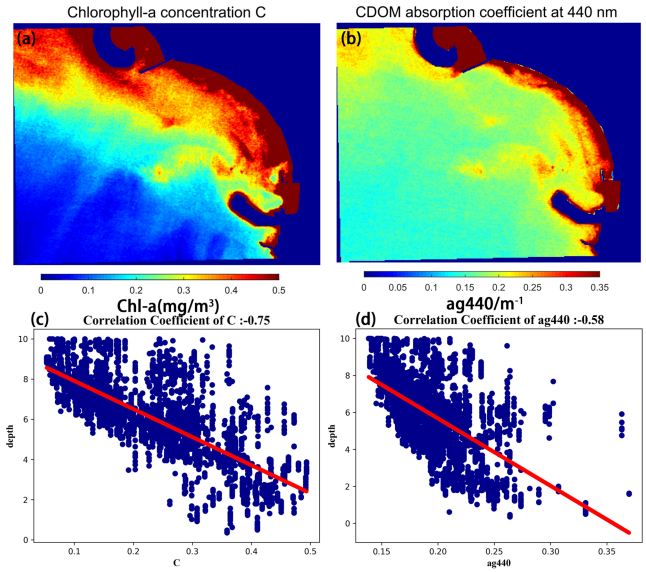

Fig. 5. Distribution and correlation regression plots of water quality factors in the port.

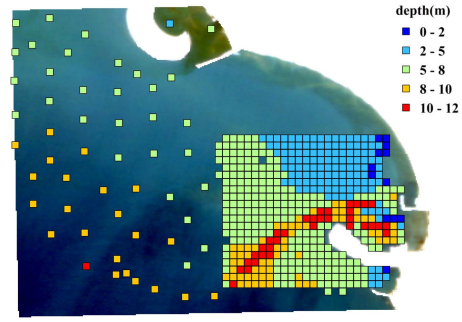

Fig. 6. Distribution of measured water depth in Nanshan port.

3) SONAR Data: From July 11, 2021 to July 13, 2021, we used the wide band multibeam system (WBMS) produced by NORBIT of Norway to survey the water depth in the experimental area in a shipborne way. The acquired water depth data exhibit a substantial quantity and a high level of precision. The plane positioning accuracy is better than 0.5 m, and the depth measurement accuracy is better than 0.2 m. We extracted a total of approximately 200 000 measurement depth point cloud data with a resolution of 5 m to generate the training and testing sets required for the study. Nanshan Port contains a vast water area and complex boundaries. To enhance the robustness of the experiment, another set of 50 control points is selected from the nautical chart (http://webapp.navionics.com) as a supplement to the whole dataset. We took 5000 water depth points from the measured water depth dataset as samples. Among those samples, 4500 points were selected as training set and the rest 500 points were selected as test set. In Fig. 6, we show the distribution of the measured sample points used in this experiment. Each point in Fig. 6 represents the mean value of the water depth control points within a range. The datum used for the water depth here is the theoretical lowest tidal level in the experimental area. This is in line with the local chart datum. To provide input images in deep learning networks, the entire dataset should have the same dimensions and spatial resolution as the in situ dataset.

B. Model Training

The subsequent model is constructed based on the flowchart, as depicted in Fig. 1, and it is categorized into two types of comparison approaches and the one proposed approach.

1) Train Model:

a) Proposed approach: CNN-based deep learning framework: CNN models have advantages in image processing, as well as statistical regression analysis. These networks can minimize an objective function and are trained to approximate a mapping between inputs and outputs. Here, we designed a two dimensions CNN-based deep learning framework to retrieve the water depth. To train the model, we registered the in situ control point with the pixel value in the multispectral images. The center pixel is viewed as weighted averages of nearby known pixels. This method considered the impact of adjacent pixels on water depth retrieval through 2-D CNN to better realize underwater terrain extraction.

We show in Fig. 7 the structure of the CNN-based deep learning framework. The convolutional kernel of our proposed model is used to extend the channels to extract more features. Pooling is used to reduce the width and height of the input data to extract important information. The rectified linear unit (ReLu) function serves as the activation function between the convolutional layer and the pooling layer, which is plotted in Fig. 7, with a yellow dashed line. Although it exhibits a linear appearance and behavior, this activation function is in fact nonlinear. Neural networks utilizing this activation function effectively mitigate the issue of vanishing gradients during the training process. The expression is given as follows:

$$f(x) = \max(0,x) \tag{14}$$

where x represents the input-independent variable and $f(x)$ represents the function value.

Unlike the conventional activation Sigmoid function, the ReLu function is less likely to cause gradient explosion or gradient disappearance. The whole operation process is optimized as the cost of the neural network is reduced by the ReLu function as well.

We used a conventional CNN-based framework with the input layer being five neurons with UQAA and three neurons without UQAA. We chose the architecture from ResNet20 [35], which is a small version of a residual architecture achieving state-of-the-art performance on many computer vision tasks. The water depth points extracted from in situ measurements were used as a priori bathymetric points. A 7×7 subimage was extracted from the multispectral image with a priori bathymetric point as the center. We introduced the input feature of size 5(or 3) $\times$ 7 $\times$ 7 (bands $\times$ width $\times$ height) into the model. The prior water depth was used as a label for model learning. The two dimensions CNN model has five layers, which contain 64, 128, 256, 256, and 512 neurons, respectively. To reduce the gradient descent, the ReLU function was used as the activation function of the

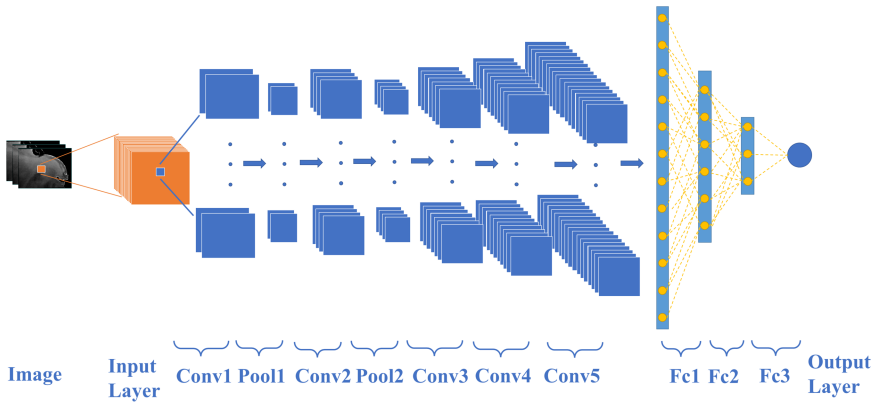

Fig. 7. CNN model structure.

hidden layers. Finally, we predicted the water depth by using the linear activation function.

In the study, we chose the strategy called minibatch to iteratively train the model [36], which helps to improve the operation efficiency of our proposed model. By dividing the training set into equal subsets as per a certain number randomly, these subsets are referred to as minibatch. This method not only solved the low operation efficiency issue but also improved the convergence speed of the network.

In the proposed network model, a for loop is adopted to traverse every minibatch data, making a gradient descent for each batch. We then update the slope parameter and intercept parameter in backpropagation. We calculated the network's prediction error via the loss function over every batch of the training set. Following the calculation of the gradient of the loss function, an optimizer was introduced for updating the different parameters of the network to reduce the loss of the model. We trained the network by using Adam [37] ($\beta 1 = 0.9$ and $\beta 2 = 0.999$), which is a standard CNN optimization method based on the stochastic gradient descent. It iterates continuously. When the iteration (epoch $= 60$ and minibatch size $= 20$) stops, the loss function converges at the same time, and the training of the model is finished.

b) Baseline: Simple BP-NN: The simple BP-NN, as a traditional artificial neural network, mimics the learning process of neurons from feedback. The simple network includes only one hidden layer. The interconnection between adjacent neurons is balanced, involving weights and bias tuned during the process of backward propagation.

We implemented the model by using Python. In the simple BP-NN, the only hidden layer was constructed involving 300 nodes, and the transfer function was the hyperbolic tangent (tanh) function. The optimizer was Adam, with a learning rate of 0.05, and the StepLR was selected as the training scheduler. Moreover, the maximum number of training, learning rate, and momentum coefficient were given by 1000, 0.05, and 0.9, respectively. Following the preposing procedures, the data were imputed into the model with bathymetric retrieval computer configuration.

c) Baseline: RF: In this integrated supervised learning model, multiple predicted outcomes are calculated, and the prediction results are studied simultaneously to improve the prediction accuracy. Self-help sampling is performed in each decision tree, and error estimation is performed by using the sample data outside the bag. The variables are randomly chosen when the decision tree is generated.

In the RF regressor, the training data contained five features (R_{rs} of red/green and blue bands) with UQAA and three features (R_{rs} of red/green and blue bands) without UQAA. We describe the setting of the RF algorithm as follows. The detailed configurations included 1000 decision trees ($n$tree), where the max depth of each tree was 50.

d) Baseline: XGBoost: XGBoost is based on the gradient boosting decision tree. It carries out the second-order Taylor expansion of the loss function by using the lifting learning algorithm. To avoid overfitting, we constructed the GridSearchCV function from the sklearn package's model_selection module in Python. By giving a value interval, we performed the search in sequence until the best combination of parameters (eta, gamma, max_depth, and n_estimators) was achieved.

Serving as an integrated learning model, the learning rate was 0.05. The maximum depth of regressors was set as 3, and the number of estimators was given by 500.

e) Baseline: SVR: SVR is a type of generalized linear classifier that performs binary classification of data with an optional supervised learning method. It can also be applied to nonlinear situations. Functional regression is realized by constructing decision functions in high-dimensional space. It is often employed to generate some multidimensional small sample regression models. In this article, radial basis function (RBF) was selected as the kernel method for regression.

The RBF was given as the kernel function searching for the optimal solution. We imported the Standscaler function from the sklearn package's preprocessing module in Python to solve the problem that the dimensions of dependent variables are different and cannot be compared.

2) Model Evaluation: The depth estimation accuracy of all models can be calculated by using the following errors:

$$\mathrm{MRE} = \left(\frac{1}{n} \sum_{i=1}^{n} \left| h_i - \hat{h}_i \right| / h_i \right) * 100\% \qquad (15)$$

$$\text{RMSE} = \left(\sum_{i=1}^{n} \left(h_i - \hat{h}_i \right)^2 / n \right)^{1/2} \tag{16}$$

$$R^2 = 1 - \frac{\sum_{i=1}^{n} \left(h_i - \hat{h}_i \right)^2}{\sum_{i=1}^{n} \left(\overline{h_i} - \hat{h}_i \right)^2} \tag{17}$$

where h_i represents the measured depth, $\hat{h}$ represents the estimated depth, and n represents the number of input data.

We performed the accuracy evaluation based on three statistical parameters, including MRE and RMSE. Lower MRE and RMSE values indicate a higher accuracy for bathymetric retrieval. RMSE quantifies the absolute error between predicted and observed values, while MRE captures the relative deviation or bias. Both metrics provide valuable insights into the performance and quality of a model's predictions. R^2 was also used to describe the model-fitting effect. A high R^2 value reflects good fitting effect of the model.

The relative bathymetric error (RBE) is adopted to capture the error at a specific position. The absolute value |RBE| is given by

$$|\text{RBE}| = \left(\left| h_i - \hat{h}_i \right| / h_i \right) * 100\%. \tag{18}$$

III. Results

To evaluate the prediction results, the assessment was carried out through two parallel experiments, and the bathymetry mapping was conducted in Section IV. These two experiments are titled "Water Depth Estimation Accuracy in Different Sizes of Dataset" and "Water Depth Estimation Accuracy in Different Datasets."

The first experiment aims to validate the optimization capability of the proposed UQAA across various dataset sizes and ensure that it does not result in adverse effects. The second experiment aims to demonstrate the superiority of the authors' proposed method over other approaches, establishing its potential for further investigation and broader application.

A. Water Depth Estimation Accuracy in Different Sizes of Dataset

In this article, the water depth control points collected by acoustic-sounding instruments were selected as the priori dataset. It is more accurate and more timely compared with spaceborne laser bathymetry. This is due to the fact that sound waves are transmitted from the transducer to the seabed and return at a very fast speed. They are not easy to be lost. We can also use sonar data to test the consistency of water depth. With the help of traditional acoustic instruments as data validation, underwater terrain extraction is more conducive. In order to deeply explore the influence of UQAA on water depth estimation accuracy, different sizes are selected as training sets, which are displayed in Fig. 8, as the *X*-axis. We observed from Fig. 8 that the accuracy with UQAA was greater than that without it in almost every model. The incorporation of the improved quantitative algorithm for aquatic applications (UQAA) enables subsequent improvements in the obtained outcomes while ensuring the mitigation of any adverse impacts.

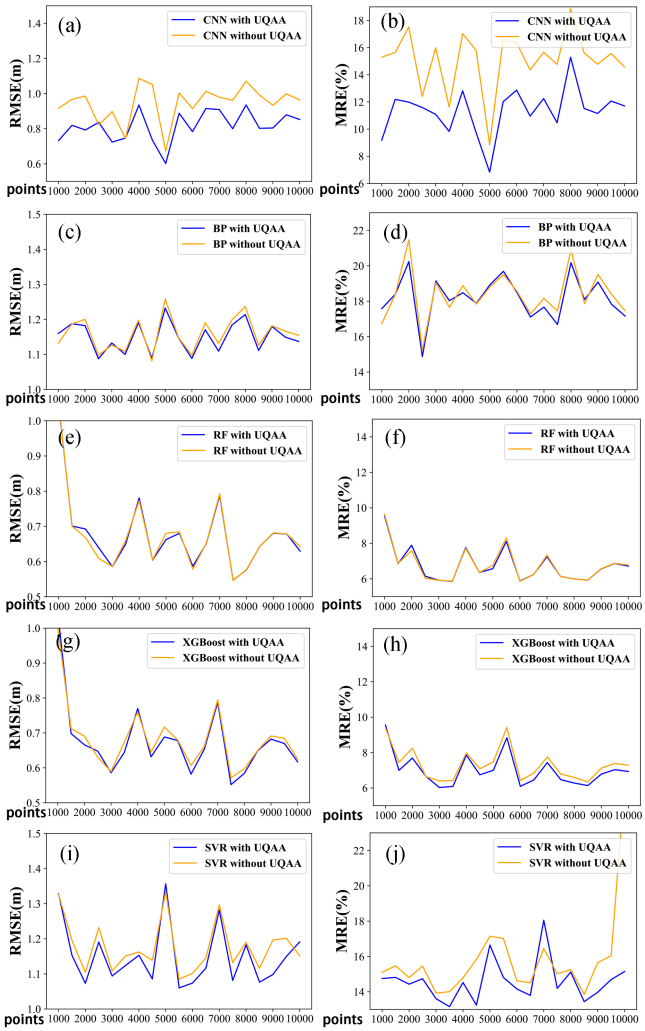

Fig. 8. Bathymetric retrieval accuracies of different algorithms are compared.

We found that the RMSEs and MREs of the BP-NN and the RF algorithm changed slightly. Along with UQAA, the RMSEs and MREs of the XGBoost algorithm and SVR algorithm have declined significantly overall. This is especially true when the number of points exceeds 6000. The accuracy of CNN was boosted, obviously, given the input of UQAA results. The RMSE and MRE of the CNN model decreased dramatically, where the RSME decreased by 23 cm and the MRE decreased by 5%. We may draw a preliminary conclusion that the UQAA results could be employed as training data for depth inversion accuracy to optimize the model.

To simulate what happens when the model encounters deep water anomalies, we added 50 deep water points extracted from the chart to the training set of 5000 measurement points (see Section III-C). When compared with other models that exhibited fluctuations in accuracy with a dataset of 5000 points, the CNN model demonstrated superior accuracy. This suggests that the model possesses robust outlier handling capabilities and effective predictive abilities.

TABLE II
COMPARISON OF DIFFERENT WATER DEPTHS AND MACHINE LEARNING METHODS

Methods	0–3 m (48 points)		3–6 m (197 points)		6–9 m (205 points)		>9 m (50 points)		Overall (500 points)	
	MRE (%)	RMSE (m)	MRE (%)	RMSE (m)	MRE (%)	RMSE (m)	MRE (%)	RMSE (m)	MRE (%)	RMSE (m)
CNN+UQAA	16.05	0.48	5.20	0.38	5.77	0.60	6.54	0.96	6.63	0.55
CNN	27.91	0.62	6.84	0.58	6.64	0.69	6.95	1.01	8.86	0.67
BP+UQAA	73.57	1.56	14.09	0.84	9.91	0.99	23.83	2.75	18.92	1.23
BP	70.28	1.47	14.44	0.91	9.96	1.00	24.57	2.83	18.81	1.26
RF+UQAA	15.31	0.83	4.89	0.46	5.45	0.64	9.72	1.13	6.60	0.67
RF	15.30	0.81	5.05	0.48	5.73	0.67	9.66	1.12	6.77	0.68
XGboost+UQAA	14.28	0.75	5.57	0.49	5.82	0.67	10.50	1.18	7.00	0.69
XGboost	15.44	0.92	6.30	0.52	5.92	0.66	10.90	1.21	7.48	0.72
SVR+UQAA	30.44	1.52	13.53	0.86	11.93	1.07	37.80	2.77	13.87	1.11
SVR	30.29	1.54	13.88	0.88	12.14	1.08	38.02	2.78	17.15	1.33

B. Water Depth Estimation Accuracy With UQAA

We utilized 500 test points with normal distribution for the test in Table II and Fig. 9. In Table II, general differences were observed between RMSE without and with UQAA for different machine learning models. They are 0.12 m (CNN), 0.03 m (BP), 0.01 m (RF), 0.03 m (XGBoost), and 0.23 m (SVR). As in the previous results, the CNN and the RF algorithm performed better in the overall test points. The XGBoost model came next. The simple BP-NN and the SVR algorithm turned out to have poor performance in this set of comparisons. Except for the section of 3–6 m, the CNN model had lower RMSE and MRE than the RF algorithm. Since the training points are normally distributed, the accuracy at both ends of the data appears to be generally poor, lacking training. Remarkably, at the end of the validation dataset, where water depth was deeper than 9 m, the CNN model error was still controlled below 1 m. We note in Fig. 9 that the red regression line is plotted on the scatter plot of correlation, compared with the black reference line. Clearly, Fig. 9(c) and (d) indicates the result of the BP-NN, and Fig. 9(i) and (j) indicates the result of the SVR algorithm. There appeared to be a large gap between the regression line and the reference line. Relatively, there was also a small gap that cannot be ignored between the regression line and the reference line in Fig. 9(g) and (h), indicating the result of the XGBoost algorithm. The gaps in Fig. 9(a) and (b), and (e) and (f) are small enough to be ignored. Their R^2 values were both over 0.9, showing good fitting ability.

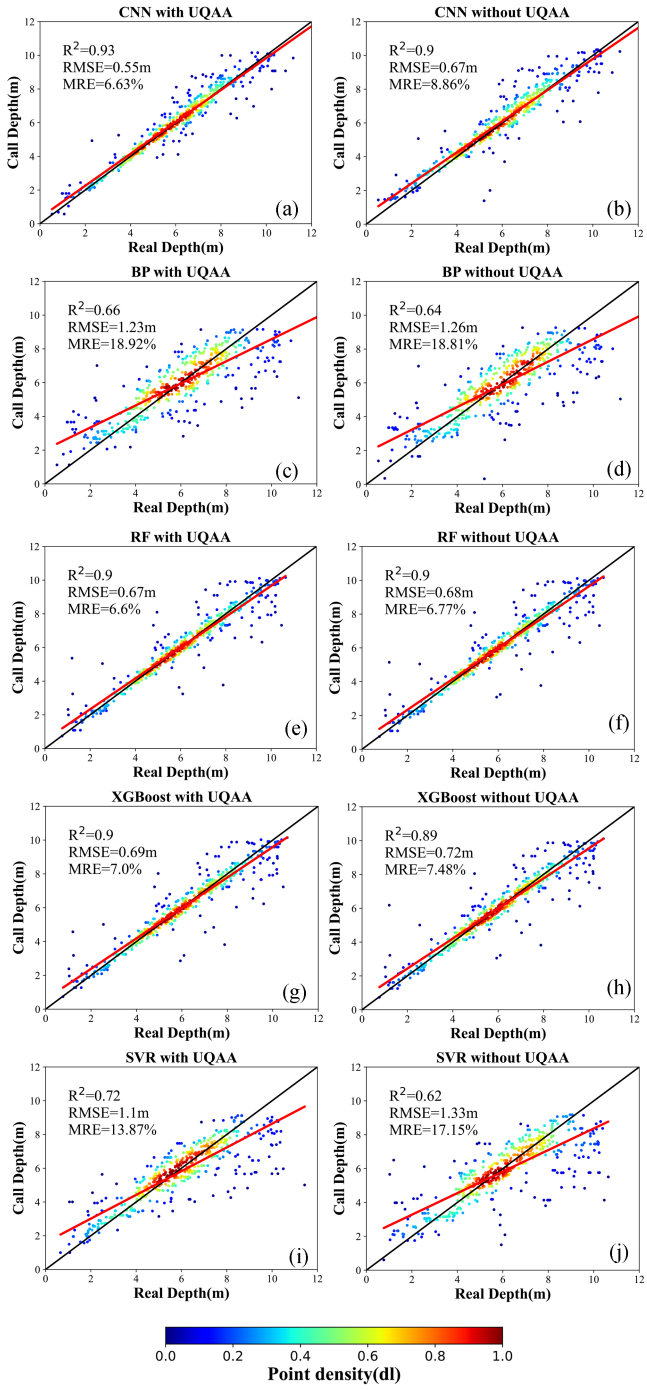

Fig. 9. Correlation between the in situ depths and the water depth estimation results based on different algorithms.

IV. DISCUSSION

The environmental conditions of Nanshan Port are characterized by turbid water. While direct application of UQAA may not be feasible, the derived water quality factors have the potential to enhance the accuracy of bathymetric inversion. This empirical model serves as a means to verify the practical applicability of the computed water quality factors for optimizing bathymetric inversion. Many factors could influence the inversion results in the depth of variable algorithms. The obtained water quality factors demonstrated their reliability for the study, as they exhibited strong spatial distribution characteristics that were closely correlated with the trend of water depth distribution.

In our two previous experiments, we have demonstrated the robustness of the UQAA method after undergoing specific optimizations, which ensures that it does not yield negative impacts on the overall results. Additionally, our observations have clearly indicated that CNN-based deep learning statistical

TABLE III
CONTRACT EXPERIMENT OF DIFFERENT KERNEL SIZES

Kernel Sizes (pixels)	RMSE (m)	MRE (%)	R^2 of validation set	R^2 of training set
9 × 9	0.576	7.733	0.925	0.892
7 × 7	0.644	7.764	0.907	0.894
5 × 5	0.554	6.963	0.925	0.892
3 × 3	0.616	7.992	0.914	0.878
1 × 1	0.884	11.029	0.824	0.820

models possess enhanced prediction and inversion capabilities, particularly when they incorporate more features compared with the traditional machine learning methods.

Moreover, it is crucial to acknowledge that the selection of model hyperparameters and the potential errors introduced during the experiment have a discernible impact on the accuracy of water depth retrieval. Furthermore, we have explored how the proposed method can be effectively applied in practical scenarios.

In this section, we will delve into the specific factors that contribute to variations in inversion results, shedding light on their implications and potential implications for future research and applications. Additionally, we will visualize the bathymetry results to demonstrate the practical feasibility of our proposed approach.

Our research aims to provide a comprehensive understanding of the factors influencing water depth retrieval accuracy, guiding the development of more robust and reliable methodologies. By addressing these challenges and refining the approach, we seek to enhance the application of our proposed method in diverse geographic regions and scenarios. Through collaboration with fellow researchers and experts, we aspire to advance the field of water depth estimation and contribute to the sustainable management of coastal environments and marine resources.

A. *Design of Model Superparameters*

In our comparative experiment, the superparameters of the machine model, including the BP-NN, RF, XGBoost, and SVR algorithm, were represented by the optimal parameters retrieved through the grid search approach [28]. The best results were taken as the comparison group. It is essential to select the convolution kernel size before model training. In Table III, we show different sizes relevant to the relationship between kernel size and model precision. Except for the size of 1×1, R^2 of other models maintained a relatively high level for the training set or validation set. The result shows that the CNN model can achieve the lowest RMSE and MRE with a kernel size of 5×5 pixels. Usually, there would be some error in convolution computation when the kernel size is too small or too large [38].

B. *Comparative Analysis of Water Depth Estimation Algorithms With the Introduction of Water Quality Factors*

Similarly, following the BOOSTING integration concept [39], the XGBoost algorithm's overall RMSE was comparable to the RF algorithm. However, the MRE was higher in the XGBoost algorithm.

In contrast, when considering the RMSE and MRE of the CNN model, the accuracy of the RF and XGBoost algorithms without UQAA appeared to be higher. Nevertheless, when incorporating UQAA results, the CNN model demonstrated marked improvement in terms of numerical values, suggesting enhanced accuracy.

Interestingly, both the RF and XGBoost algorithms exhibited consistent RMSE and MRE values, with or without the input of UQAA results. The RMSE initially decreased and then stabilized within the range of 0.5–0.8 m. The MRE fluctuated between 6% and 10%.

When dealing with a limited number of calibration points in practical applications, the results obtained for water depth retrieval were also noteworthy. The accuracy of the BP-NN and CNN models started to increase in the dataset containing 1000–2000 points, and the improvement became more evident after introducing UQAA. The CNN model showed better accuracy, particularly with less than 1500 input points, and this was further enhanced with the inclusion of UQAA results. The influence of different training sets on the overall results is expected, and it is worth noting that the variable training algorithm with UQAA demonstrated higher accuracy compared with the algorithm without UQAA.

We demonstrated the superiority of the CNN model with UQAA results across different training set sizes, highlighting its potential and efficacy for water depth estimation.

C. *Error Analysis of SDB and* In Situ *Measurement*

The bathymetry error comes from the GF-6 WFV image and the field data provided by the multibeam sonar. First, the impact of water surface anomalies on the overall inversion results cannot be completely removed, although preprocessing operations, including the sunlight correction, have been performed for the GF-6 WFV image. Second, the spatial resolution of the GF-6 satellite is 16 m, whereas the spatial resolution of the multibeam sonar measurement is only 0.5 m. This yields errors in matching water depth points with image pixel points without considering positioning errors [40]. In addition, the quality factors of a water body are derived by analyzing the R_{rs} of the water surface combined with the empirical coefficient. This indicates that there could be some errors in areas under complex water conditions. Third, it is difficult to synchronize field measurements with other remote-sensing data. It is conducive to model construction and accuracy evaluation by taking the in situ measurement data as prior data. However, since it is difficult to synchronize in the time dimension, inevitably, there will be accuracy errors between the inversion value and true value.

To address these challenges, Hong et al. [41] proposed a novel spectral mixture model to address spectral variability for hyperspectral unmixing, which is the problem of estimating the abundance maps of different materials from hyperspectral imagery. Spectral variability refers to the variations of spectral signatures of the same material due to various factors. The proposed model overcomes the limitations of the classical linear mixing

model, which assumes that the spectral signatures are fixed and known. The model models the main spectral variability (i.e., scaling factors) separately by using an endmember dictionary, which contains the spectral signatures of different materials. It then models the other spectral variabilities by using a spectral variability dictionary, which contains the deviations from the endmember dictionary. The model applies a data-driven learning strategy to learn both dictionaries from the hyperspectral data, by using a low-coherence prior knowledge, which assumes that the atoms of the two dictionaries are not similar to each other. The model also estimates the abundance maps simultaneously by using a reconstruction strategy, which minimizes the difference between the observed data and the model output. The article claims that the model can achieve higher accuracy and lower errors than the state-of-the-art methods on synthetic and real datasets by effectively reducing the spectral variability and capturing the spatial–spectral features of the hyperspectral data.

We believe that the ALMM method is relevant and effective for our research, and we plan to explore the possibility of incorporating it into our framework to further optimize the data quality and obtain better inversion results in the future. We expect that by using the ALMM method, we can reduce the errors caused by spectral variability and improve the accuracy and robustness of our method.

D. Spatial Distribution of RBEs

The spatial distribution of RBEs reveals the direction of improving inversion accuracy and the difference in retrieval results under different algorithms. We show in Fig. 10(a), (c), and (e) the red symbols for the absolute RBEs, which are greater than 30%, yellow symbols for the absolute RBEs, which are in 20%–30%, light blue symbols for the absolute RBEs, which are in 10%–20% interval, and dark blue symbols for the absolute RBEs, which are less than 10%. In Fig. 10(a) and (c), we calculated the distribution of absolute RBEs by the CNN model with UQAA and without UQAA. Without UQAA, the number of points in absolute RBEs over 10% (color light blue, red, and yellow) area increased. We observed from Fig. 10(b) and (d) that there was a correlation distribution map between absolute RBEs and real water depth. In the trained models, the high point density area is between 5 and 7 m, whereas absolute RBEs were mostly lower than 10%. Moreover, the CNN model with UQAA results has more concentrated areas of high point density between 5 and 7 m. The corresponding absolute RBE was less than 5%. In Fig. 10(a) and (c), we observed that the distribution of both maps was similar, especially in absolute RBEs above 10% region. The accuracy of northeast part was lower than that of the other parts. Regarding remote-sensing sounding, the overestimation often occurred in the shallow area near the port. The underestimation always occurred in the deep area away from the port [8]. This phenomenon was in line with the result of Fig. 10(a) and (c). However, it was relatively improved in favor of UQAA results.

To verify the universality of the model, another dataset of 5000 points was introduced into the CNN model for validation. The result is shown in Fig. 10(e). Although the spatial distribution of Fig. 10(e) from the new 5000 points showed more points of high

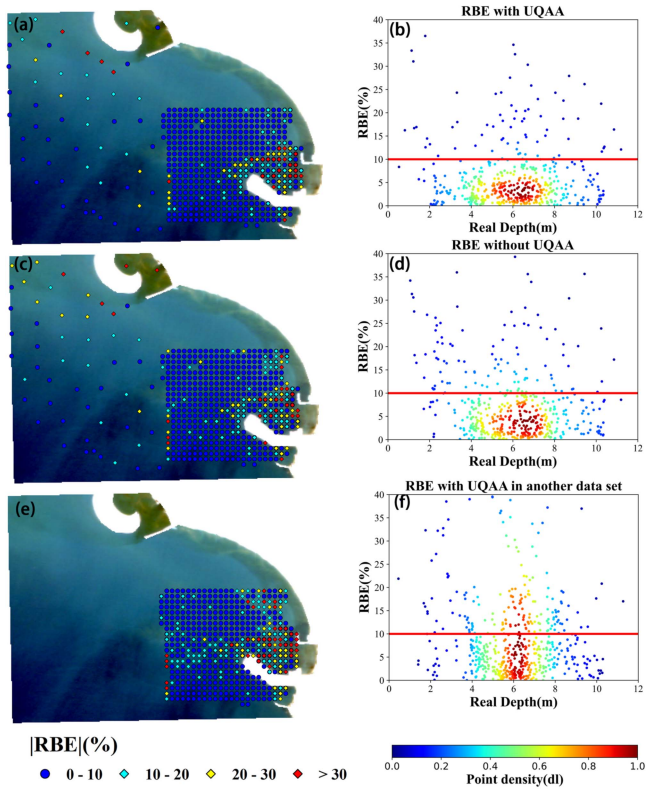

Fig. 10. Spatial distribution of RBEs and correlation distribution with different algorithms and different dataset. (a) and (b) were with UQAA. (c) and (d) were without UQAA input. (e) and (f) was with another data set of 5000 points.

absolute RBE, they had the same overall trends of distribution. Given that a part of the points was input to train the model in Fig. 10(a), it was expected that Fig. 10(a) had lower errors than Fig. 10(e), and there were many points with high point density over the line of 10% RBE, as shown in Fig. 10(f). In Fig. 10(e), we observed little difference between the results produced by the two datasets since the error points were mainly concentrated in shallow-water areas. Different sample points influenced the result, but they had a small impact on the result of space distribution. Multidimensional data input with spatial information, such as UQAA results, showed a greater impact on the model inversion effect compared with similar data from different sets.

E. Bathymetry Maps of Models

To figure out how well this method performs in practical applications, we introduced large-scale images with no a priori data into three previously trained models in Fig. 11. We observed significant visual differences between the results of the CNN and the other two models. The CNN model showed a relatively shallow depth distribution, which is close to the actual situation.

1) Bathymetry With Priori Data: From priori data, despite the actual presence of relatively deep water near the port, the depth estimation obtained from the CNN model showed an unexpectedly higher value. This discrepancy highlights a drawback associated with the CNN model. However, it is important to note that both the RF and XGBoost algorithms exhibited similar

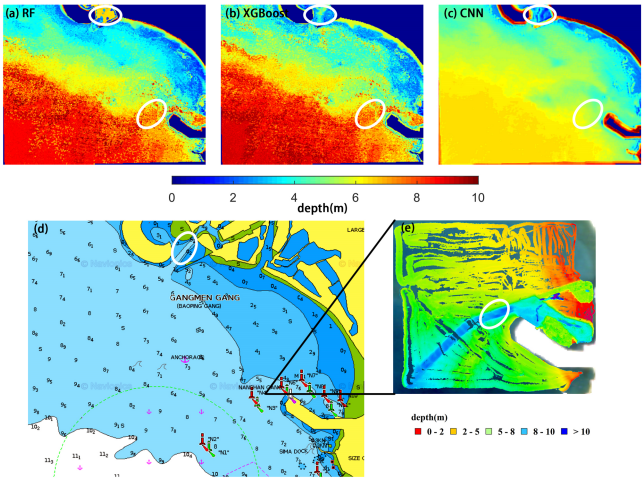

Fig. 11. Bathymetry maps at a large spatial scale. (a) Was the RF algorithm with UQAA. (b) Was the XGBoost algorithm with UQAA. (c) Was the CNN model with UQAA. (d) Was from nautical chart. (e) Was from NORBIT system.

spatial patterns, with a tendency toward deeper water depths near the port as well. The average water depth of the CNN model in a deep water area was about 7 m, which was close to the chart data, as displayed in Fig. 11(d) and (e). We show in Fig. 11(d), acquired from the nautical chart, the gentle variation of water depth distribution, which is more like the map of the CNN model.

In Fig. 11(d), there is almost no water area near Nanshan Port that exceeds 10 m, except for an artificial channel in the middle. Machine learning models based on the mathematical and statistical principles have poor learning of outlier water depth. This phenomenon becomes apparent in the maps generated by the RF and XGBoost algorithms, leading to an overestimation of the overall water depths, surpassing the actual values. In contrast, the performance of the CNN model reveals the presence of the waterway, although its depth is underestimated compared with the measured values. However, it is worth noting that the overall depth of the waterway aligns more closely with the actual value at the same time.

2) Bathymetry Without Priori Data: To further validate the predictive power of the model for no-prior data, it was found that there was an estuary outside the measured data area in the north part of Fig. 11(d). It can be set as a standard to measure the prediction ability of the model in an unknown area. In Fig. 11(a), the water depth in this area was incorrect. The estuary can be displayed in Fig. 11(b) and (c).

RMSE is an important quantitative index to measure the accuracy of water depth inversion. However, RMSE is greatly impacted by the distribution of validation points. In areas lacking accurate validation data, it can only be verified by comparing the nautical chart. Although the CNN model has some deviation in the inversion of localized high values, it still shows a strong prediction ability and can be used in the actual thematic products.

V. Conclusion

In this article, we proposed the idea of combining a UQAA with a CNN-based deep learning framework to estimate the water depth and extract underwater terrain data automatically. By using the UQAA, a map of water quality factors was drawn in Fig. 6. This was strongly related to the bottom brightness implying the water depth information. We extracted the bathymetric points from the in situ measured data by the WBMS system to train the CNN model with preprocessed GF-6 images and derived water quality factors. We considered four classic methods as baselines. We also discussed and evaluated the accuracy of bathymetry for different training sets and different algorithms.

To verify the performance of the proposed method, we compared the inversion data results and image results with the validation data. They had been divided before and had no input into model training. Our comparison indicated that the CNN model with UQAA can outperform all the baselines with or without UQAA input, with the RMSE being 0.55, the MRE being 6.63%, and the R^2 being 0.93 when the number of training set was 5000. In general, when the number of training points was between 1000 and 10 000, the results of bathymetry with UQAA results were better than those without UQAA results. The accuracy of water depth retrieval, especially in our proposed CNN model, can be improved by considering the spatial distribution and numerical analysis of the water quality parameters.

Moreover, we analyzed the spatial distribution of errors between the estimated depth and the measured depth. We found that introducing UQAA results as feature data can decrease the errors in the shallow area near the port. The inversion feasibility of the CNN model with UQAA was tested in areas lacking accurate verification data as well. Generally speaking, in actual surveying and mapping, we pay more attention to the accuracy of the results. Considering the accuracy advantages and growth potential brought by deep learning, applying deep learning models to bathymetry is of great research value. Moreover, due to experimental conditions, we can only use the GPU of our laptop for inversion calculations. If we use a server cluster, we can further reduce the time cost of deep learning.

For future research, more optical parameters obtained through QAA could be inputted into deep learning neural network model and applied to remote-sensing images with higher spatial resolution. These retrieval results could be applied to port management and underwater terrain acquisition. Moreover, the following directions could be explored for further improvement.

1) Other types of remote-sensing data, such as thermal infrared, microwave, or LiDAR, could be investigated to complement the optical data and provide more information for water depth estimation and underwater terrain extraction.
2) The effects of different environmental factors, such as water turbidity, sun glint, cloud cover, or wave height, could be examined on the accuracy and robustness of the proposed method, and adaptive strategies could be developed to cope with these challenges.
3) The CNN-based deep learning framework and the UQAA could be optimized by using more advanced network architectures, loss functions, regularization techniques, or data augmentation methods to enhance the feature extraction and fusion capabilities of the method.

4) The proposed method could be applied to other regions or scenarios that require accurate bathymetric maps, such as coastal erosion monitoring, coral reef conservation, marine habitat mapping, or underwater archaeology.

REFERENCES

[1] S. J. Purkis et al., "High-resolution habitat and bathymetry maps for 65,000 sq. km of Earth's remotest coral reefs," *Coral Reefs*, vol. 38, pp. 467–488, 2019, doi: 10.1007/s00338-019-01802-y.

[2] J. Horta, A. Pacheco, D. Moura, and Ó. Ferreira, "Can recreational echosounder-Chartplotter systems be used to perform accurate nearshore bathymetric surveys?," *Ocean Dyn.*, vol. 64, no. 11, pp. 1555–1567, 2014, doi: 10.1007/s10236-014-0773-y.

[3] J. Hedley, C. Roelfsema, and S. Phinn, "Efficient radiative transfer model inversion for remote sensing applications," *Remote Sens. Environ.*, vol. 113, no. 11, pp. 2527–2532, 2009, doi: 10.1016/j.rse.2009.07.008.

[4] A. Dekker et al., "Intercomparison of shallow water bathymetry, hydro-optics, and benthos mapping techniques in Australian and Caribbean coastal environments," *Limnol. Oceanogr. Methods*, vol. 9, no. 9, pp. 396–425, 2011, doi: 10.4319/lom.2011.9.396.

[5] I. Caballero, R. Stumpf, and A. Meredith, "Preliminary assessment of turbidity and chlorophyll impact on bathymetry derived from Sentinel-2A and Sentinel-3A satellites in South Florida," *Remote Sens.*, vol. 11, no. 6, 2019, Art. no. 645, doi: 10.3390/rs11060645.

[6] T. Sagawa, Y. Yamashita, T. Okumura, and T. Yamanokuchi, "Satellite derived bathymetry using machine learning and multi-temporal satellite images," *Remote Sens.*, vol. 11, no. 10, 2019, Art. no. 1155, doi: 10.3390/rs11101155.

[7] V. Mateo-Perez, M. Corral-Bobadilla, F. Ortega-Fernandez, and E. P. Vergara-Gonzalez, "Port bathymetry mapping using support vector machine technique and sentinel-2 satellite imagery," *Remote Sens.*, vol. 12, no. 13, Jul. 2020, Art. no. 2069, doi: 10.3390/rs12132069.

[8] J. Zhong, J. Sun, Z. L. Lai, and Y. Song, "Nearshore bathymetry from ICESat-2 LiDAR and sentinel-2 imagery datasets using deep learning approach," *Remote Sens.*, vol. 14, no. 17, Sep. 2022, Art. no. 4229, doi: 10.3390/rs14174229.

[9] T. Hoeser, F. Bachofer, and C. Kuenzer, "Object detection and image segmentation with deep learning on Earth observation data: A review—Part II: Applications," *Remote Sens.*, vol. 12, no. 18, Sep. 2020, Art. no. 3053, doi: 10.3390/rs12183053.

[10] T. Hoeser and C. Kuenzer, "Object detection and image segmentation with deep learning on Earth observation data: A review—Part I: Evolution and recent trends," *Remote Sens.*, vol. 12, no. 10, May 2020, Art. no. 1667, doi: 10.3390/rs12101667.

[11] L. Ma, Y. Liu, X. Zhang, Y. Ye, G. Yin, and B. A. Johnson, "Deep learning in remote sensing applications: A meta-analysis and review," *ISPRS J. Photogramm. Remote Sens.*, vol. 152, pp. 166–177, 2019, doi: 10.1016/j.isprsjprs.2019.04.015.

[12] Z. Chen, G. Wu, H. Gao, Y. Ding, D. Hong, and B. Zhang, "Local aggregation and global attention network for hyperspectral image classification with spectral-induced aligned superpixel segmentation," *Expert Syst. Appl.*, vol. 232, 2023, Art. no. 120828.

[13] Z. Chen, D. Hong, and H. Gao, "Grid network: Feature extraction in anisotropic perspective for hyperspectral image classification," *IEEE Geosci. Remote Sens. Lett.*, vol. 20, Jul. 2023, Art. no. 5507105, doi: 10.1109/LGRS.2023.3297612.

[14] D. Hong, L. Gao, J. Yao, B. Zhang, A. Plaza, and J. Chanussot, "Graph convolutional networks for hyperspectral image classification," *IEEE Trans. Geosci. Remote Sens.*, vol. 59, no. 7, pp. 5966–5978, Jul. 2021.

[15] X. Cao, X. Fu, C. Xu, and D. Meng, "Deep spatial-spectral global reasoning network for hyperspectral image denoising," *IEEE Trans. Geosci. Remote Sens.*, vol. 60, Apr. 2021, Art. no. 5504714, doi: 10.1109/TGRS.2021.3069241.

[16] X. Wu, D. Hong, and J. Chanussot, "Convolutional neural networks for multimodal remote sensing data classification," *IEEE Trans. Geosci. Remote Sens.*, vol. 60, Nov. 2021, Art. no. 5517010, doi: 10.1109/TGRS.2021.3124913.

[17] Z. Chen et al., "Global to local: A hierarchical detection algorithm for hyperspectral image target detection," *IEEE Trans. Geosci. Remote Sens.*, vol. 60, Dec. 2022, Art. no. 5544915, doi: 10.1109/TGRS.2022.3225902.

[18] M. El-Diasty, "Satellite-based bathymetric modeling using a wavelet network mode," *ISPRS Int. J. Geo-Inf.*, vol. 8, no. 9, Sep. 2019, Art. no. 405, doi: 10.3390/ijgi8090405.

[19] B. Wilson, N. C. Kurian, A. Singh, and A. Sethi, "Satellite-derived bathymetry using deep convolutional neural network," in *Proc. IEEE Int. Geosci. Remote Sens. Symp.*, 2020, pp. 2280–2283.

[20] M. Al Najar et al., "Coastal bathymetry estimation from sentinel-2 satellite imagery: Comparing deep learning and physics-based approaches," *Remote Sens.*, vol. 14, no. 5, 2022, Art. no. 1196, doi: 10.3390/rs14051196.

[21] B. Chen, Y. Yang, D. Xu, and E. Huang, "A dual band algorithm for shallow water depth retrieval from high spatial resolution imagery with no ground truth," *ISPRS J. Photogramm. Remote Sens.*, vol. 151, pp. 1–13, 2019.

[22] W. Yang, B. Matsushita, K. Yoshimura, J. Chen, and T. Fukushima, "A modified semianalytical algorithm for remotely estimating euphotic zone depth in turbid inland waters," *IEEE J. Sel. Topics Appl. Earth Observ. Remote Sens.*, vol. 8, no. 4, pp. 1545–1554, Apr. 2015, doi: 10.1109/JSTARS.2015.2415853.

[23] X. Zhang, Y. Ma, and J. Zhang, "Shallow water bathymetry based on inherent optical properties using high spatial resolution multispectral imagery," *Remote Sens.*, vol. 12, no. 18, 2020, Art. no. 3027.

[24] R. Huang, K.-F. Yu, Y. Wang, J. Wang, L. Mu, and W. Wang, "Bathymetry of the coral reefs of Weizhou island based on multispectral satellite images," *Remote Sens.*, vol. 9, no. 7, 2017, Art. no. 750, doi: 10.3390/rs9070750.

[25] Z. Wu, Z. Mao, W. Shen, D. Yuan, X. Zhang, and H. Huang, "Satellite-derived bathymetry based on machine learning models and an updated quasi-analytical algorithm approach," *Opt. Express*, vol. 30, pp. 16773–16793, 2022, doi: 10.1364/OE.456094.

[26] X. Zhao et al., "Water deep mapping from HJ-1B satellite data by a deep network model in the sea area of Pearl River Estuary, China," *Open Geosci.*, vol. 13, pp. 782–795, 2021, doi: 10.1515/geo-2020-0267.

[27] V. Mateo-Perez, M. Bobadilla, F. Ortega-Fernández, and V. Montequín, "Determination of water depth in ports using satellite data based on machine learning algorithms," *Energies*, vol. 14, no. 9, 2021, Art. no. 2486, doi: 10.3390/en14092486.

[28] W. Shen, Y. Rao, Q. Ji, R. Meng, and K. F. Luan, "Shallow sea remote sensing water depth inversion based on 'grid search+XGBoost' algorithm," *Remote Sens. Inf.*, vol. 37, no. 1, pp. 14–18, 2022.

[29] J. D. Hedley, A. R. Harborne, and P. J. Mumby, "Technical note: Simple and robust removal of sun glint for mapping shallow-water benthos," *Int. J. Remote Sens.*, vol. 26, no. 10, pp. 2107–2112, 2005, doi: 10.1080/01431160500034086.

[30] G. Doxani, M. Papadopoulou, P. Lafazani, M. Tsakiri, and E. Mavridou, "Sun glint correction of very high spatial resolution images," *Thales, in Honor of Prof. Emeritus Michael E. Contadakis*, pp. 329–340, Jan. 2013.

[31] P. Smith, "Bilinear interpolation of digital images," *Ultramicroscopy*, vol. 6, no. 2, pp. 201–204, 1981.

[32] J. P. Chavez, G. Berlin, and L. Sowers, "Statistical method for selecting landsat MSS ratios," *J. Appl. Photograph. Eng.*, vol. 8, pp. 23–30, 1984.

[33] Z. Lee, "Visible-infrared remote sensing model and applications for ocean waters," Ph.D. dissertation, Dept. Marine Sci., Univ. of South Florida, Tampa, FL, USA, 1994.

[34] L. Hui, P. Furnace, T. Bangyi, S. Liang, K. Linchong, and Z. Hansong, *J. Oceanogr. (Chin. Version)*, vol. 31, no. 2, pp. 57–62, 2009.

[35] K. He, X. Zhang, S. Ren, and J. Sun, "Deep residual learning for image recognition," in *Proc. IEEE Conf. Comput. Vis. Pattern Recognit.*, 2016, pp. 770–778.

[36] E. Bøhn, S. Moe, and T. Johansen, "On the effects of properties of the mini-batch in reinforcement learning," in *Proc. Int. Conf. Intell. Technol. Appl.*, Berlin, Germany, 2022, pp. 71–80, doi: 10.1007/978-3-031-10525-8_6.

[37] B. Raharjo, N. Farida, P. Subekti, R. Siburian, P. Heka Ardana, and R. Rahim, "Optimization forecasting using back-propagation algorithm," *J. Appl. Eng. Sci.*, vol. 19, no. 4, pp. 1083–1089, 2021, doi: 10.5937/jaes0-30175.

[38] J.-B. Kong and J. Minseok, "Association analysis of convolution layer, kernel and accuracy in CNN," *J. Korea Inst. Electron. Commun. Sci.*, vol. 14, no. 6, pp. 1153–1160, 2019, doi: 10.13067/jkiecs.2019.14.6.1153.

[39] R. E. Schapire, "A brief introduction to boosting," in *Proc. 16th Int. Joint Conf. Artif. Intell.*, 1999, pp. 1401–1406.

[40] H. Ni, W. Wang, Q. Ren, L. Lu, J. Wu, and L. Ma, "Model-based sediment characterization using multibeam angular backscatter data," in *Proc. IEEE/MTS Oceans Seattle Conf.*, 2019, pp. 1–4, doi: 10.23919/OCEANS40490.2019.8962831.

[41] D. Hong, N. Yokoya, J. Chanussot, and X. X. Zhu, "An augmented linear mixing model to address spectral variability for hyperspectral unmixing," *IEEE Trans. Image Process.*, vol. 28, no. 4, pp. 1923–1938, Apr. 2019.

Wei Shen received the Ph.D. degree in cartography and geographic information system from Beijing Normal University, Beijing, China, in 2007.

He is currently a Professor and master's supervisor with the College of Marine Science, Shanghai Ocean University, Shanghai, China, the Head of the Marine Surveying and Mapping major, and a member of the Marine Surveying and Mapping Professional Committee of the Chinese Society of Surveying and Mapping. His research interests include marine surveying and mapping, GIS, RS, LIDAR, underwater information detection and processing, and virtual reality and simulation. Over the past five years, he has authored or coauthored 25 papers in domestic and foreign core journals (including 7 international indexed papers).

Muyin Chen is currently working toward the M.Sc. degree in marine sciences with Shanghai Ocean University, Shanghai, China.

His research interests include the application of deep learning to marine remote sensing optical data.

Zhongqiang Wu (Member, IEEE) received the M.Sc. degree in marine sciences from Shanghai Ocean University, Shanghai, China, in 2016, and the Ph.D. degree in geography from Nanjing University, Nanjing, China, in 2022.

He is currently a Lecturer with the School of Information Science and Technology, Hainan Normal University, Haikou, China. His research interests include ocean remote sensing and remote-sensing-based bathymetry.

Jiaqi Wang is currently working toward the M.Sc. degree in marine sciences with Shanghai Ocean University, Shanghai, China.

His research interests include the application of machine learning to marine remote sensing optical data.